Angular momentum transport by heat-driven g-modes in slowly pulsating B stars

R. H. D. Townsend,[1,2][⋆] J. Goldstein[1,2] and E. G. Zweibel[1]

[1] *Department of Astronomy, University of Wisconsin-Madison, Madison, WI 53706, USA*

[2] *Kavli Institute for Theoretical Physics, University of California, Santa Barbara, CA 93106, USA*

ABSTRACT

Motivated by recent interest in the phenomenon of waves transport in massive stars, we examine whether the heat-driven gravity (g) modes excited in slowly pulsating B (SPB) stars can significantly modify the stars' internal rotation. We develop a formalism for the differential torque exerted by g modes, and implement this formalism using the GYRE oscillation code and the MESASTAR stellar evolution code. Focusing first on a $4.21 M_\odot$ model, we simulate 1 000 yr of stellar evolution under the combined effects of the torque due to a single unstable prograde g mode (with an amplitude chosen on the basis of observational constraints), and diffusive angular momentum transport due to convection, overshooting, and rotational instabilities. We find that the g mode rapidly extracts angular momentum from the surface layers, depositing it deeper in the stellar interior. The angular momentum transport is so efficient that by the end of the simulation, the initially non-rotating surface layers are spun in the retrograde direction to ≈ 30 per cent of the critical rate. However, the additional inclusion of magnetic stresses in our simulations almost completely inhibits this spin-up. Expanding our simulations to cover the whole instability strip, we show that the same general behaviour is seen in all SPB stars. After providing some caveats to contextualize our results, we hypothesize that the observed slower surface rotation of SPB stars (as compared to other B-type stars) may be the direct consequence of the angular momentum transport that our simulations demonstrate.

Key words: asteroseismology – stars: evolution – stars: interiors – stars: massive – stars: oscillations – stars: rotation.

1 INTRODUCTION

Slowly pulsating B (SPB) stars are a class of variable main-sequence B-type stars first recognized by Waelkens (1991). They are characterized by photometric and spectroscopic variations with periods on the order of days, caused by the excitation of one or more of the star's gravity (g) modes. The excitation mechanism is an opacity peak at a temperature $T \approx 200\,000$ K arising from same K-shell bound–bound transitions of iron and nickel (e.g. Dziembowski, Moskalik & Pamyatnykh 1993); this 'iron bump' serves as the valve in the heat-engine process first envisaged by Eddington (1926) as the driver of classical Cepheid pulsations.

In this paper, we explore to what extent the heat-driven g modes in SPB stars can extract angular momentum from one part of the star and deposit it in another. The phenomenon of wave transport of angular momentum is well studied in the context of lower mass stars (e.g. Schatzman 1993; Kumar & Quataert 1997; Zahn, Talon & Matias 1997; Talon, Kumar & Zahn 2002; Talon & Charbonnel 2005; Rogers, MacGregor & Glatzmaier 2008), and a number of authors explore whether the same process might be important in more-massive stars. Rogers et al. (2013) and Rogers (2015) use two-dimensional anelastic hydrodynamical simulations to investigate the impact of internal gravity waves (IGWs), excited stochastically at the convective core boundary, on the internal rotation profile of massive stars. Lee et al. (2014) consider whether the same IGWs can supply the necessary angular momentum to form the episodic decretion disc seen in the rapidly rotating Be star HD 51452.

A couple of studies also consider angular momentum transport by heat-driven g modes, as opposed to stochastic IGWs: Lee (2013) examines the Be-star decretion disc problem, whereas Lee, Mathis & Neiner (2016) consider the meridional flows that can be established by the modes. However, the conclusions reached in both of these papers were limited in scope by the inability to predict mode amplitudes from

linear perturbation theory. In this work, we sidestep this issue by using empirical constraints on amplitudes, derived from observations. Such constraints have been employed previously when considering stochastic IGWs (e.g. Lee et al. 2014, in the context of Be stars; Belkacem et al. 2015, in the context of red giant stars). In this context, they allow us to explore whether the heat-driven g modes *that we actually see in SPB stars* can appreciably influence the stars' internal rotation.

In the following section, we lay out the theoretical formalism that serves as the basis for our analysis. In Section 3, we simulate angular momentum transport by a single g mode in a representative SPB star model. In Section 4, we then expand the scope of our simulations to encompass the whole SPB instability strip. Finally, we summarize and discuss our findings in Section 5.

2 FORMALISM

2.1 Differential torque

Starting with the azimuthal component of the momentum conservation equation, Lee & Saio (1993) derive an equation governing the transport of angular momentum by small-amplitude non-axisymmetric waves,

$$\frac{\partial j}{\partial t} = -\frac{1}{r^2}\frac{\partial}{\partial r}\left(r^2\Psi\right) - \frac{\partial}{\partial t}\left\langle r\sin\theta\,\overline{\rho'v'_\phi}\right\rangle - \left\langle\overline{\rho'\frac{\partial\Phi'}{\partial\phi}}\right\rangle. \tag{1}$$

Here, t is the time coordinate and (r, θ, ϕ) are the radial, polar, and azimuthal coordinates in a spherical system; (v_r, v_θ, v_ϕ) are the corresponding components of the fluid velocity vector $\boldsymbol{v}$; ρ, and Φ are the density and gravitational potential, respectively,

$$j \equiv \left\langle r\sin\theta\,\rho v_\phi\right\rangle \tag{2}$$

is the mean angular momentum density, and

$$\Psi \equiv \left\langle r\sin\theta\left(\rho\,\overline{v'_\phi v'_r} + v_\phi\,\overline{\rho'v'_r} + \overline{\rho'v'_\phi v'_r}\right)\right\rangle \tag{3}$$

the mean angular momentum flux carried by the waves. Angle brackets $\langle\ldots\rangle$ denote averages over θ and overbars $\overline{\ldots}$ are averages over ϕ. Primes indicate Eulerian perturbations, whereas the absence of a prime implies an equilibrium quantity. The three terms on the right-hand side of equation (1) represent the contributions towards the spherically averaged torque density $\partial j/\partial t$ arising, respectively, from the divergence of the wave flux, from the growth or decay of the angular momentum stored in the waves themselves, and from self-gravitation.

In this work, we adopt a simplified form of these expressions. We drop the second and third terms on the right-hand side of the flux equation (3). The second term represents mass transport via Stokes drift, and in the steady state a system of return currents not modelled by equation (1) will arise that cancel this term (see, e.g. Fuller & Lai 2014); while the third term is third-order in perturbed quantities, and therefore makes a negligible contribution at small perturbation amplitudes. We likewise neglect the second term on the right-hand side of the transport equation, as this term vanishes for steady-state pulsation. Combining (1) and (3), the simplified equation governing angular momentum transport then becomes

$$\frac{\partial j}{\partial t} = -\frac{1}{r^2}\frac{\partial}{\partial r}\left(r^2\rho\left\langle r\sin\theta\,\overline{v'_\phi v'_r}\right\rangle\right) - \left\langle\overline{\rho'\frac{\partial\Phi'}{\partial\phi}}\right\rangle. \tag{4}$$

Introducing the differential torque

$$\frac{\partial\tau}{\partial r} = 4\pi r^2\frac{\partial j}{\partial t}, \tag{5}$$

representing the rate of change of angular momentum in a spherical shell of unit thickness, we can also write the transport equation as

$$\frac{\partial\tau}{\partial r} = -\frac{\partial}{\partial r}\left(4\pi r^2\rho\left\langle r\sin\theta\,\overline{v'_\phi v'_r}\right\rangle\right) - 4\pi r^2\left\langle\overline{\rho'\frac{\partial\Phi'}{\partial\phi}}\right\rangle. \tag{6}$$

2.2 Torque due to an oscillation mode

We now evaluate the differential torque exerted by a single non-radial oscillation mode, whose angular dependence is described by the spherical harmonic $Y_\ell^m(\theta, \phi)$ with harmonic degree ℓ and azimuthal order m. The perturbations arising due to this mode are expressed as

$$\xi_r(r, \theta, \phi; t) = Re\left[\sqrt{4\pi}\,\tilde{\xi}_r(r)Y_\ell^m(\theta, \phi)\exp(-\mathrm{i}\sigma t)\right],$$

$$\boldsymbol{\xi}_{\mathrm{h}}(r, \theta, \phi; t) = Re\left[\sqrt{4\pi}\,\tilde{\xi}_h(r)r\nabla_{\mathrm{h}}Y_\ell^m(\theta, \phi)\exp(-\mathrm{i}\sigma t)\right],$$

$$f'(r, \theta, \phi; t) = Re\left[\sqrt{4\pi}\,\tilde{f}'(r)Y_\ell^m(\theta, \phi)\exp(-\mathrm{i}\sigma t)\right].$$

$$\tag{7}$$

Here, f stands for any perturbable scalar, whereas ξ_r is the radial component of the displacement perturbation vector $\boldsymbol{\xi}$, $\boldsymbol{\xi}_h$ is the corresponding horizontal (polar and azimuthal) part of this vector, and ∇_h is the horizontal part of the spherical-polar gradient operator. The velocity perturbation follows from $\boldsymbol{\xi}$ as

$$\boldsymbol{v}' = \frac{\partial \boldsymbol{\xi}}{\partial t}. \tag{8}$$

The tilded quantities $\tilde{\xi}_r$, $\tilde{\xi}_h$, $\tilde{f}'$ are the complex eigenfunctions determined from solution of the non-adiabatic pulsation equations (see Appendix B), and σ is the associated complex eigenfrequency. Based on the negative sign appearing in the time exponents in equation (7), modes with positive (negative) m propagate in the direction of increasing (decreasing) ϕ.

Substituting the above expressions into equation (6), and using equations (B1–B3) to eliminate radial derivatives, leads to

$$\frac{\partial \tau}{\partial r} = 2\pi m r^2 \mathrm{Im}\left[\frac{\sigma}{\sigma^*} \left(\frac{\delta\tilde{\rho}}{\rho} \tilde{P}'^* + \tilde{\rho}'\tilde{\Phi}'^* + g\tilde{\xi}_r \tilde{\rho}'^* \right) - \tilde{\rho}'\tilde{\Phi}'^* \right], \tag{9}$$

where P is the pressure, $g \equiv \mathrm{d}\Phi/\mathrm{d}r$ is the gravitational acceleration, an asterisk indicates the complex conjugate, and δ denotes the Lagrangian perturbation. As usual, Eulerian ($\tilde{f}'$) and Lagrangian ($\delta\tilde{f}$) perturbations associated with any scalar quantity f (assumed spherically symmetric in the equilibrium state) are linked by the relation

$$\delta\tilde{f} = \tilde{f}' + \frac{\mathrm{d}f}{\mathrm{d}r}\tilde{\xi}_r. \tag{10}$$

Because we are interested in steady-state pulsation, we have dropped the exponential growth/decay factor $\exp(2\sigma_{\mathrm{I}} t)$ from equation (9), where σ_{I} is the imaginary part of the eigenfrequency. Consistency might seem to dictate that the factor σ/σ^* inside the brackets also be eliminated; however, such a step would lead to undesirable consequences, as we now demonstrate.

2.3 Conservation of total angular momentum

In an isolated star, wave transport may redistribute angular momentum, but it can never alter the star's total angular momentum. To examine whether the differential torque (6) respects this conservation constraint, we integrate it to find the total torque on the star,

$$\tau \equiv \int_0^{R_*} \frac{\mathrm{d}\tau}{\mathrm{d}r}\,\mathrm{d}r = -\left[4\pi r^2 \rho \left\langle r\sin\theta\,\overline{v_\phi' v_r'} \right\rangle \right]_{r=R_*} - \frac{1}{4\pi G}\left[4\pi r^2 \left\langle \overline{\frac{\partial\Phi'}{\partial r}\frac{\partial\Phi'}{\partial\phi}} \right\rangle \right]_{r=R_*}. \tag{11}$$

Here, we make use of the linearized Poisson equation (B4) to eliminate the density perturbation ρ'. The first term on the right-hand side corresponds to the surface angular momentum luminosity of the star, whereas the second represents the external gravitational torque on the star. If there is no mass above the stellar surface, then both terms vanish – the first due to the density dropping to zero and the second because the gravitational potential perturbation above the surface must be a (bounded) solution to Laplace's equation. Accordingly, for an isolated star, the global torque τ is identically zero, and we confirm that the star's total angular momentum is conserved during wave transport.

Turning to equation (9), we now demonstrate that eliminating the factor σ/σ^* (with the purported goal of consistency) leads to a spurious global torque. Following Ando (1983),[1] we split the differential torque (9) into two components: a steady-state ('ss') part that is always present and a transient ('tr') part that vanishes as $\sigma_{\mathrm{I}} \to 0$. Thus,

$$\frac{\partial\tau}{\partial r} = \left.\frac{\partial\tau}{\partial r}\right|_{\mathrm{ss}} + \left.\frac{\partial\tau}{\partial r}\right|_{\mathrm{tr}}, \tag{12}$$

where

$$\left.\frac{\partial\tau}{\partial r}\right|_{\mathrm{ss}} = 2\pi m r^2 \mathrm{Im}\left[\frac{\delta\tilde{\rho}}{\rho}\delta\tilde{P}^* \right] \tag{13}$$

and

$$\left.\frac{\partial\tau}{\partial r}\right|_{\mathrm{tr}} = 2\pi m r^2 \mathrm{Im}\left[\left(\frac{\sigma}{\sigma^*} - 1 \right)\left(\frac{\delta\tilde{\rho}}{\rho}\tilde{P}'^* + \tilde{\rho}'\tilde{\Phi}'^* + g\tilde{\xi}_r\tilde{\rho}'^* \right) \right]. \tag{14}$$

The steady-state differential torque can also be written as

$$\left.\frac{\partial\tau}{\partial r}\right|_{\mathrm{ss}} = -\frac{m}{2\pi}\frac{\mathrm{d}W}{\mathrm{d}r}, \tag{15}$$

where

$$\frac{\mathrm{d}W}{\mathrm{d}r} = -4\pi^2 r^2 \mathrm{Im}\left[\frac{\delta\tilde{\rho}}{\rho}\delta\tilde{P}^* \right] \tag{16}$$

is the differential work representing the change in mode energy per unit radius over one cycle (see, e.g. Castor 1971; Ando & Osaki 1977; note that the minus sign here arises from our choice of time dependence in equation 7).

---

[1] Note that Ando uses the symbol τ for the torque density $\partial j/\partial t$, rather than the more-common usage adopted here.

Table 1. Parameters for the stellar model considered in Section 3.

M_* ($M_\odot$)	R_* ($R_\odot$)	L_* ($L_\odot$)	T_{eff} (K)	X_c	Age (Myr)
4.21	4.41	542	13 300	0.260	135

Integrating equation (12) leads to a global torque

$$\tau = \tau_{ss} + \tau_{tr}, \tag{17}$$

where

$$\tau_{ss} = \int_0^{R_*} \left.\frac{\partial \tau}{\partial r}\right|_{ss} dr \qquad \text{and} \qquad \tau_{tr} = \int_0^{R_*} \left.\frac{\partial \tau}{\partial r}\right|_{tr} dr. \tag{18}$$

Combining equations (15) and (18), the steady-state torque becomes

$$\tau_{ss} = -\frac{m}{2\pi} \int_0^{R_*} \frac{dW}{dr} dr = -\frac{m}{2\pi} W, \tag{19}$$

where the second equality defines the total work W. Using equation (25.17) of Unno et al. (1989), this is further transformed into

$$\tau_{ss} = -2m \frac{\sigma_I}{\sigma_R} E_W, \tag{20}$$

where σ_R is the real part of σ and E_W is the time-averaged total energy of oscillation. From this expression, it is clear that the steady-state torque is non-zero whenever σ_I is non-zero.

Returning now to equation (9), we note that eliminating the σ/σ^* factor (by setting it to unity) is equivalent to dropping the transient components in equations (12) and (17). Via the latter equation, the global torque will then equal the steady-state torque, and accordingly be non-zero whenever σ_I is non-zero. This violation of total angular momentum conservation is undesirable, and so we choose to keep the σ/σ^* factor in equation (9).

3 ANGULAR MOMENTUM TRANSPORT IN AN SPB STAR

We now apply the formalism developed in the previous section to explore angular momentum transport in a $4.21 M_\odot$ stellar model that we choose as representative of SPB stars (the specific motivation for this choice will be given later, in Section 4).

3.1 Stellar model

We construct the model using public release 9575 of the MESASTAR stellar evolution code (Paxton et al. 2011, 2013, 2015), with OPAL opacity tables and proto-solar abundances from Asplund et al. (2009). Rotation is for the time being neglected, and convection is treated using the Schwarzschild stability criterion, a mixing-length parameter $\alpha_{MLT} = 1.5$, and an exponential overshoot parameter $f_{ov} = 0.024$. The model evolution is started on the pre-main sequence and continued until the central hydrogen mass fraction has dropped to $X_c = 0.260$. The model's fundamental parameters – including its mass M_*, radius R_*, luminosity L_*, and effective temperature T_{eff} – are summarized in Table 1, and its position within the SPB instability strip on the Hertzsprung–Russell (HR) diagram can be seen in Fig. 7.

3.2 Pulsation modes

We use version 5.0 of the GYRE oscillation code to evaluate eigenfrequencies and eigenfunctions of the model's $\ell = 1$ and $\ell = 2$ g modes. Compared to the initial release of GYRE described by Townsend & Teitler (2013), version 5.0 incorporates improvements that permit fully non-adiabatic calculations (see Appendix A for details). We find that the iron bump excites $\ell = 1$ g modes with radial orders[2] $\tilde{n}$ in the interval $[-47, -22]$, and $\ell = 2$ g modes with radial orders in the interval $[-57, -22]$.

Fig. 1 illustrates the displacement eigenfunctions for the $\ell = 1$ g_{30} mode (i.e. with radial order $\tilde{n} = -30$). This mode has a dimensionless eigenfrequency $\omega = 0.229$ (see equation B21 for the definition of ω), corresponding to a period $\Pi = 2.28$ d. The normalized growth rate

$$\eta \equiv \frac{W}{\int_0^{R_*} \left|\frac{dW}{dr}\right| dr} \tag{21}$$

(e.g. Stellingwerf 1978) of the g_{30} mode is the largest among the unstable $\ell = 1$ g modes, reaching $\eta = 0.183$; however, the mode is otherwise unremarkable.

The figure shows that the fluid displacements generated by the mode are predominantly horizontal ($|\tilde{\xi}_h| \gg |\tilde{\xi}_r|$), as is typical for the high-order g modes excited in SPB stars. The imaginary parts of the eigenfunctions depart appreciably from zero only in the outer part of the

---

[2] Determined using the Takata (2006) extension to the standard Eckart–Osaki–Scuflaire classification scheme described, e.g. by Unno et al. (1989).
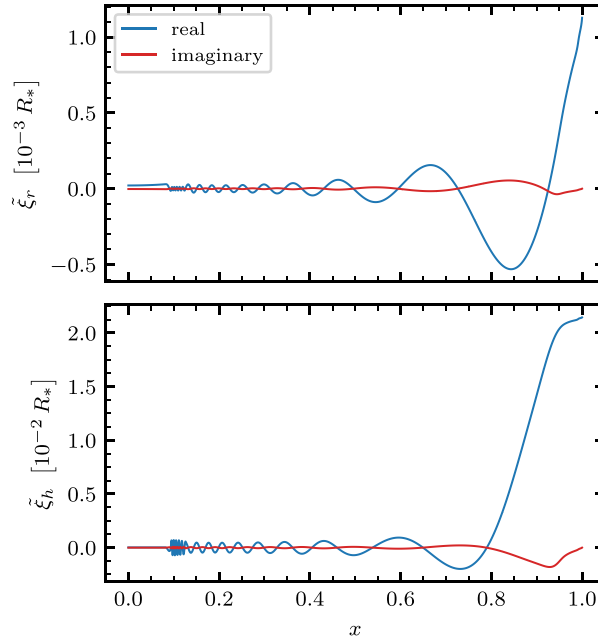
Figure 1. Displacement eigenfunctions for the $\ell = 1\,g_{30}$ mode of the $4.21M_{\odot}$ model discussed in Section 3, plotted as a function of dimensionless radius $x \equiv r/R_*$. The upper panel shows the real and imaginary parts of the radial ($\tilde{\xi}_r$) eigenfunction, and the lower panel shows the real and imaginary parts of the horizontal ($\tilde{\xi}_h$) eigenfunction.

star ($x \gtrsim 0.7$), where the thermal time-scale is short enough for non-adiabatic effects to become important. The highly oscillatory behaviour of both $\tilde{\xi}_r$ and $\tilde{\xi}_h$ in the region $0.09 \lesssim x \lesssim 0.13$ just outside the convective core arises from the steep molecular weight gradient left behind by the retreating core boundary.

Linear theory does not dictate the normalization of the eigenfunctions plotted in Fig. 1, and in most contexts this issue is of little concern, as long as the perturbations remain small. However, in order to obtain quantitatively meaningful results from the formalism presented in Section 2, a physically reasonable normalization must be chosen. As we mention in Section 1, we use observations to constrain this choice. In their analysis of 31 SPB stars observed by ground-based telescopes, Szewczuk & Daszyńska-Daszkiewicz (2015) identify the modes responsible for the stars' $\approx$10 mmag photometric variability, and determine the surface radial amplitudes ε ($\equiv \sqrt{4\pi}|\tilde{\xi}_r/R_*|$ at $x = 1$, in the present notation) for these modes. Their fig. 7 plots the distribution of these radial amplitudes; from this distribution, we estimate a 50th percentile amplitude of $\varepsilon \approx 0.004$. Unless otherwise explicitly noted, we adopt this normalization for all calculations in this paper. In the particular case of the g_{30} mode plotted in Fig. 1, the normalization results in the mode having a surface equatorial velocity amplitude of $2.6\,\mathrm{km\,s^{-1}}$ in the azimuthal direction and $0.16\,\mathrm{km\,s^{-1}}$ in the radial direction – both much smaller than the photospheric adiabatic sound speed $\approx 16\,\mathrm{km\,s^{-1}}$.

3.3 Differential torque

Fig. 2 illustrates the differential torque (9) for the prograde[3] sectoral ($m = \ell$) variant of the $\ell = 1\,g_{30}$ mode introduced above, together with the decomposition into steady-state and transient components discussed in Section 2.3. In the outer part of the star ($x \gtrsim 0.75$), the differential torque is dominated by the steady-state component, which via equation (15) varies as $-1/2\pi$ times the differential work. Thus, in the iron bump excitation zone ($x \approx 0.94$), where $\mathrm{d}W/\mathrm{d}x > 0$, the differential torque is negative; but in the radiative damping zone interior to the iron bump ($0.77 \lesssim x \lesssim 0.92$), where $\mathrm{d}W/\mathrm{d}x < 0$, the torque is positive.

Physically, these opposing torques arise because the prograde wave extracts angular momentum from the excitation zone, causing it to recoil in the retrograde direction; this angular momentum is then deposited in the damping zone, driving it in the prograde direction. In fact, only around two-thirds of the angular momentum from the excitation zone ends up in the damping zone; the remaining one-third is distributed throughout the inner envelope ($0.1 \lesssim x \lesssim 0.75$) by the action of the transient component $\mathrm{d}\tau/\mathrm{d}r|_{\mathrm{tr}}$ of the differential torque. This component is associated with the phenomenon of wave transience (e.g. Dunkerton 1981), and arises due to the fact that particle motions are not strictly periodic when $\sigma_{\mathrm{I}} \neq 0$. In a real star pulsating at a steady, finite amplitude, this component vanishes, replaced by the differential torque associated with the non-linear damping that prevents further mode growth. We cannot model this damping with linear theory (although see Gastine & Dintrans 2008a,b, for recent progress in non-linear modelling), and so caution must be exercised in interpreting the distribution of angular momentum deposition in the inner envelope.

---

[3] Since we are referring to a non-rotating star, 'prograde' in this context simply means in the direction of increasing azimuth ϕ.
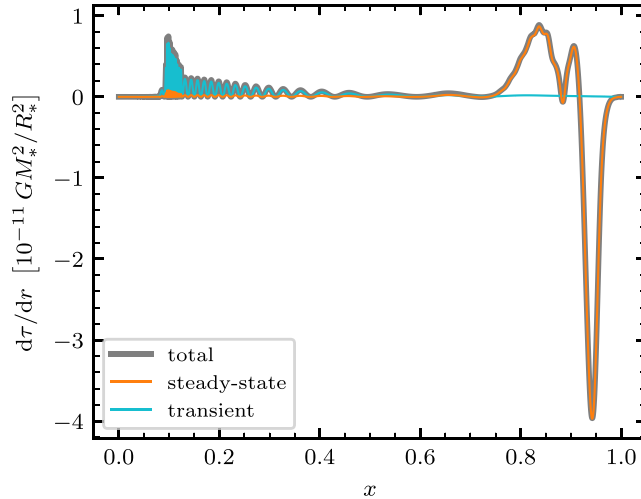
Figure 2. The differential torque exerted by the $\ell = m = 1\,\mathrm{g}_{30}$ mode of the $4.21\mathrm{M}_\odot$ model discussed in Section 3, plotted as a function of dimensionless radius $x \equiv r/R_*$. The steady-state and transient contributions towards the torque are also plotted.

3.4 Transport simulations

3.4.1 Base simulations

We now explore how the torque plotted in Fig. 2 will drive the $4.21\mathrm{M}_\odot$ model away from its initially non-rotating state. With rotation enabled via the `new_rotation_flag` and `change_rotation_flag` controls, we use MESASTAR to simulate 10^3 additional years of the star's evolution. During this evolution, the angular velocity profile[4] changes under the combined effects of the steady differential torque produced by the $\ell = m = 1\,\mathrm{g}_{30}$ mode (incorporated using MESASTAR's `other_torque` hook) and the time-dependent diffusive angular momentum transport described by equation B4 of Paxton et al. (2013). In the latter, the effective diffusion coefficient combines contributions from convection, overshooting, Eddington–Sweet circulation,[5] rotationally induced instabilities, and magnetic stresses from the fields generated by the Tayler–Spruit (TS) dynamo (see section 6 of Paxton et al. 2013). The efficacy of the TS dynamo remains a topic of ongoing debate (see, e.g. Spruit 2002; Denissenkov & Pinsonneault 2007; Zahn, Brun & Mathis 2007), and we therefore perform two simulations: for our 'magnetic' simulation, the dynamo is enabled in MESASTAR, and for the 'non-magnetic' one, it is turned off.

Fig. 3 plots the resulting angular velocity profiles $\Omega(r)$ at selected times t after the simulation start, in units of the Roche critical angular velocity $\Omega_{\mathrm{crit}} = (8GM_*/27R_*^3)^{1/2}$ (for the parameters given in Table 1, $\Omega_{\mathrm{crit}} = 7.6 \times 10^{-5}\,\mathrm{rad\,s^{-1}}$). After 1 yr, the angular velocity profiles in both non-magnetic (left-hand panel) and magnetic (right-hand panel) cases look similar: The star is spun in the retrograde ($\Omega < 0$) direction in the excitation zone at $x \approx 0.94$ and in the prograde direction in the damping zone interior to this. By $t = 10$ yr, however, the angular velocities in the outer parts of the star ($x \gtrsim 0.5$) begin to diverge.

In the non-magnetic simulation, the g_{30} mode quickly establishes a retrograde surface layer, reaching $|\Omega| \approx 0.3\,\Omega_{\mathrm{crit}}$ at the $t = 10^3$ yr mark. This surface layer is separated from the prograde stellar interior by a shear layer extending downwards from the base of the excitation zone. Towards later times, this shear layer propagates inwards into the star, but the angular velocity gradient within the layer remains approximately constant (compare, e.g. the $t = 10^2$ and 10^3 yr curves), due to a dynamical balance struck between angular momentum transport by the mode (which tries to steepen the shear) and diffusive transport (which tries to flatten it). In the magnetic simulation, the behaviour seen at later times is quite different. The field stresses greatly boost the efficiency of diffusive angular momentum transport, and the g_{30} mode is unable to establish and maintain an appreciable shear layer near the surface. Retrograde surface rotation still arises, but it never becomes significant – even after 10^3 yr, $|\Omega|$ is only $\lesssim 1$ per cent of the critical rate.

3.4.2 Comparison against Diffusive Transport

The rotation profile established by the g_{30} mode in the non-magnetic wave-transport simulation (Fig. 3, left-hand panel) is unlike the profiles typically encountered when diffusive angular momentum transport processes act alone. To illustrate this, we use MESASTAR to evolve a $4.21\mathrm{M}_\odot$ model with the inclusion of diffusive transport but without any wave transport, from an initial state of uniform rotation at the zero-age main sequence (ZAMS) until the effective temperature drops to $13\,300\,\mathrm{K}$ (cf. Table 1). Fig. 4 compares the equatorial rotation

---

[4] As with most other modern stellar evolution codes that incorporate rotation (e.g. Meynet & Maeder 1997; Heger, Langer & Woosley 2000), MESASTAR adopts the ansatz by Zahn (1992) that strong horizontal turbulence due to the stable stratification in radiative regions maintains a 'shellular' rotation profile, with the angular velocity $\Omega \equiv v_\phi/r\sin\theta$ depending only on r.

[5] Although Eddington–Sweet circulation is generally considered to be a large-scale advective process (e.g. Zahn 1992), MESASTAR treats it diffusively, following the approach described by Heger et al. (2000).
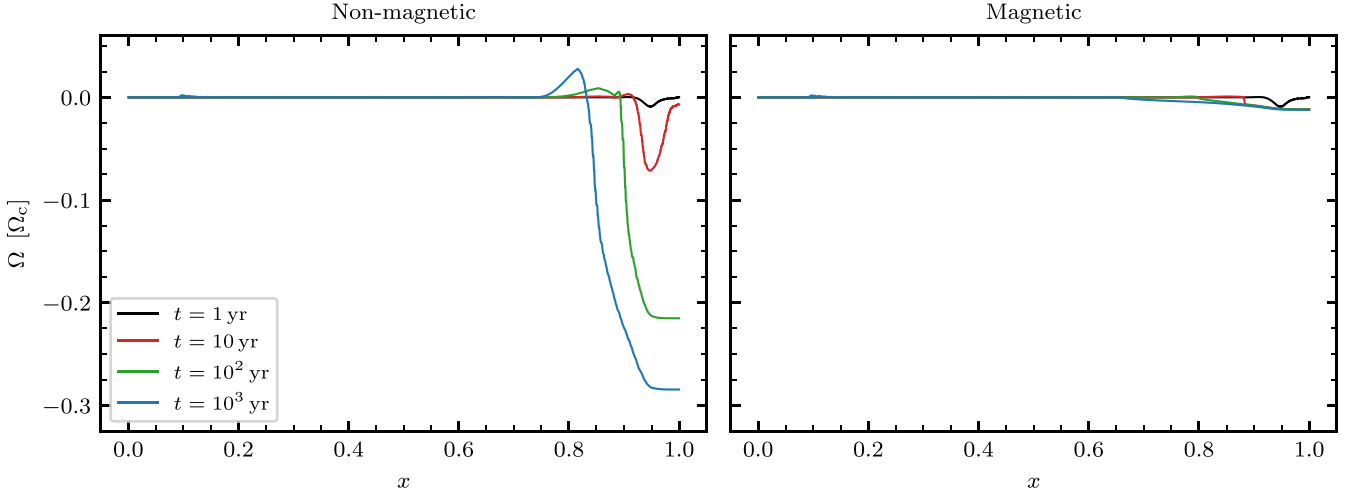
Figure 3. Snapshots at four selected times t of the angular velocity Ω of the $4.21M_\odot$ model as modified by the $\ell = 1\,g_{30}$ mode (Fig. 1), plotted as a function of dimensionless radius $x \equiv r/R_*$. The left (right-hand) panel shows results from the non-magnetic (magnetic) simulations.
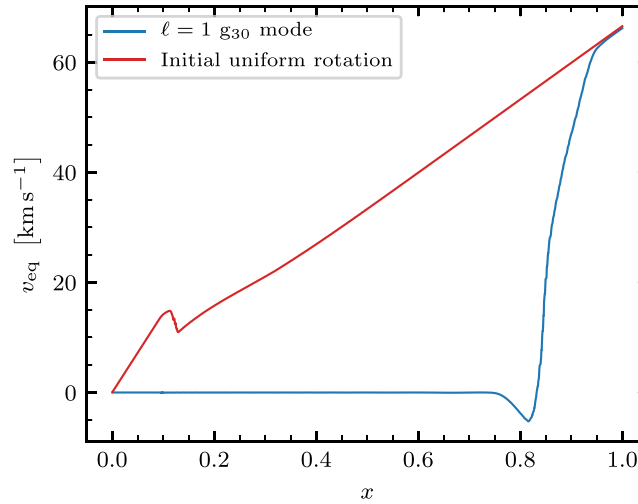

Figure 4. The equatorial rotation velocity v_{eq} of the $4.21M_\odot$ model, as modified by the $\ell = 1\,g_{30}$ mode after a time $t = 10^3$ yr and as arising from initial uniform rotation, plotted as a function of dimensionless radius $x \equiv r/R_*$.

velocity profile $v_{eq}(r) = -r\,\Omega(r)$ (the minus sign is to ensure positive surface velocities) for the wave-transport simulation at $t = 10^3$ yr against the corresponding profile of this rotating model. The initial surface equatorial velocity $v_{eq,*} = v_{eq}(R_*) = 84\,\mathrm{km\,s^{-1}}$ of the rotating model is tuned so that the surface rotation at the evolution endpoint matches the $v_{eq,*} = 66\,\mathrm{km\,s^{-1}}$ seen in the simulation.

The two velocity profiles are very similar in the superficial layers of the star, but below $x \approx 0.95$, they diverge. The equatorial velocity in the wave transport simulation changes rapidly to negative values across the near-surface shear layer, before dropping to zero for $x \lesssim 0.75$. In the rotating model, the velocity follows an approximate $v_{eq} \propto r$ relation in both core and envelope, consistent with near-uniform rotation in each region; a small shear layer across $0.09 \lesssim x \lesssim 0.13$ arises from the inhibition of diffusive angular momentum transport by the molecular weight gradient there.

3.4.3 Impact of normalization

To examine how our simulations are sensitive to the canonical mode amplitude $\varepsilon = 0.004$ adopted in Section 3.2, we repeat them for amplitudes $0 \le \varepsilon \le 0.01$ (corresponding to the range covered in fig. 7 of Szewczuk & Daszyńska-Daszkiewicz 2015). Fig. 5 summarizes these calculations by plotting the surface equatorial rotation velocity $v_{eq,*}$ at $t = 10^3$ yr as a function of ε. Although the torque scales quadratically with pulsation amplitude (see, e.g. equation 9), the surface velocity is far less sensitive to amplitude: For both curves plotted in the figure, the approximate scaling is $v_{eq,*} \propto \varepsilon^{0.8}$. We conjecture that such behaviour arises because the diffusive angular momentum transport processes also play a role in determining $v_{eq,*}$, and these processes depend non-linearly on the angular velocity and its radial derivatives.

Fig. 5 assures us that the outcome of the non-magnetic simulations is reasonably insensitive to our choice $\varepsilon = 0.004$ for the mode amplitude. At the same time, it shows that no matter how high we set this amplitude in the magnetic simulations, the spin-up of the stellar
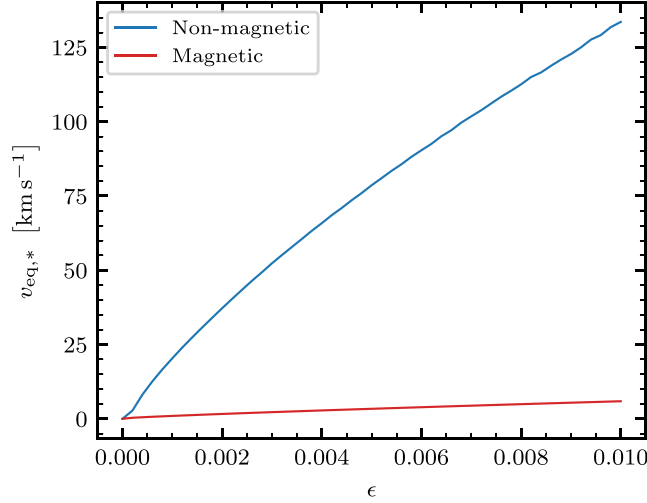
Figure 5. The surface equatorial rotation velocity $v_{\mathrm{eq},*}$ of the $4.21\mathrm{M}_\odot$ model, as modified by the $\ell = 1\, g_{30}$ mode after a time $t = 10^3$ yr, plotted as a function of amplitude parameter ε. Separate curves show the non-magnetic and magnetic cases.
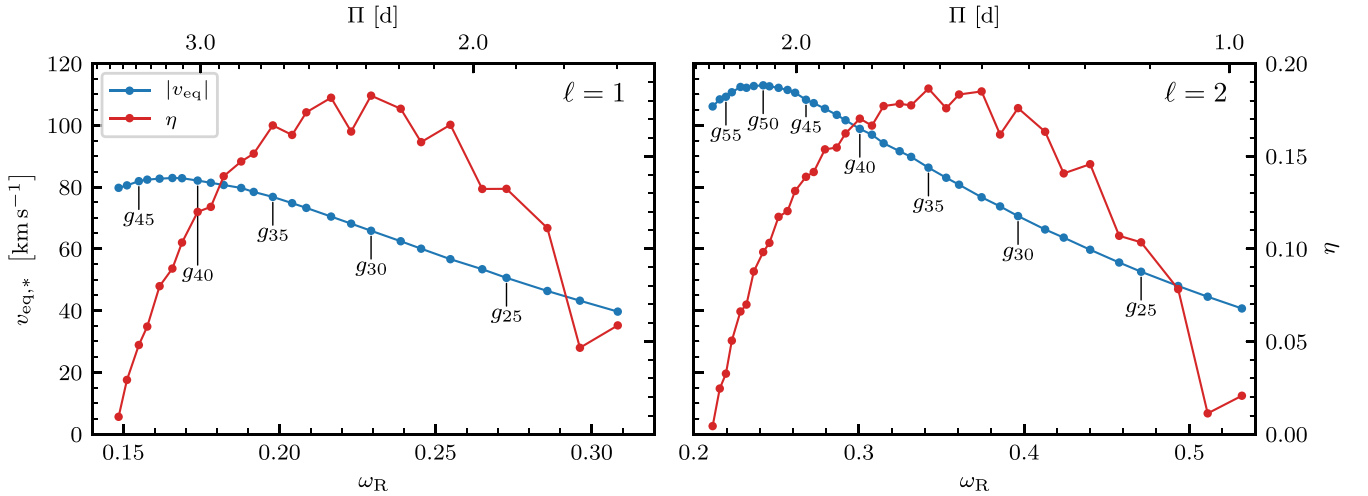

Figure 6. The surface equatorial rotation velocity $v_{\mathrm{eq},*}$ of the $4.21\mathrm{M}_\odot$ model, as modified by unstable $\ell = 1$ (left-hand panel) and $\ell = 2$ (right-hand panel) g modes after a time $t = 10^3$ yr, plotted as a function of the real part ω_{R} of the modes' dimensionless eigenfrequency. The corresponding periods Π are indicated along the top axes. Selected modes are labelled, and the normalized growth rates η are also shown using the axes to the right.

surface layers remains inhibited by the magnetic stresses. With the latter point in mind, we henceforth focus only on non-magnetic cases. However, we shall briefly return to the issue of magnetic inhibition in Section 5.

3.4.4 Impact of mode choice

To explore whether the results above generalize to other g modes of the $4.21\mathrm{M}_\odot$ model, we repeat the non-magnetic angular momentum transport simulations for all unstable $\ell = m = 1$ and $\ell = m = 2$ modes. Fig. 6 summarizes these calculations, plotting the surface equatorial rotation velocities at $t = 10^3$ yr as a function of the real part ω_{R} of the modes' dimensionless eigenfrequency. The periods

$$\Pi = \frac{2\pi}{\omega_{\mathrm{R}}} \sqrt{\frac{R_*^3}{GM_*}} \tag{22}$$

corresponding to these eigenfrequencies are indicated along the top axes. Also shown for comparison are the corresponding normalized growth rates η evaluated using equation (21), and selected modes are labelled.

In both $\ell = 1$ and $\ell = 2$ cases, the figure reveals that $v_{\mathrm{eq},*}$ increases towards lower frequencies, eventually reaching a maximum near the low-frequency limit of the instability. The behaviour of η is rather different; it is close to zero at the low- and high-frequency limits (by definition), but maximal around the frequency midpoint between these limits. To explain both behaviours, we decompose the total work W into contributions from excitation (W_+) and damping (W_-) zones:

$$W = W_+ - W_-, \tag{23}$$

where

$$W_\pm = \int_0^{R_*} \max \left(\pm \frac{\mathrm{d}W}{\mathrm{d}r}, 0 \right) \mathrm{d}r. \tag{24}$$

As we discuss in Section 3.3, the differential torque in the outer part of the star mirrors the differential work. We can therefore expect the net torque on the surface layers, where $\mathrm{d}W/\mathrm{d}x > 0$, to scale with W_+. Both W_+ and W_- increase towards lower frequencies, due to stronger Lagrangian pressure and density perturbations that boost the differential work via equation (16), and it therefore follows that the torque on the surface layers will be larger at lower frequencies, driving these layers to higher velocities as seen in the figure.

The normalized growth rate behaves differently because it scales not with W_+ or W_- but the (normalized) difference between them; rewriting equation (21),

$$\eta = \frac{W_+ - W_-}{W_- + W_-}. \tag{25}$$

Thus, although at low frequencies both W_+ and W_- are large (indicating a significant torque), they are also nearly equal to each other, leading to growth rates that are close to zero. For instance, the $\ell = 1$ g_{47} mode drives a surface velocity $v_{\mathrm{eq}, *} = 80\,\mathrm{km\,s^{-1}}$, close to the maximum for dipole modes, despite being almost neutrally stable with $\eta = 0.009$.

Comparing the two panels of Fig. 6 reveals that the $\ell = m = 2$ modes are somewhat more effective at transporting angular momentum than the $\ell = m = 1$ modes. This is simply a consequence of the factor m in the expression (9) for the differential torque, that itself comes from the azimuthal derivatives in equations (1) and (7). The dependence of $v_{\mathrm{eq}, *}$ on m is slower than linear, but this is unsurprising given the sub-linear variation with ε already discussed in Section 3.4.3.

4 ANGULAR MOMENTUM TRANSPORT ACROSS THE SPB STRIP

We now expand the scope of our simulations to encompass the SPB stars as an entire class. We use MESASTAR to construct 30 evolutionary tracks in the initial mass range $2.4\mathrm{M}_\odot \leq M \leq 9.0\,\mathrm{M}_\odot$, with each track extending from the pre-main sequence to beyond the terminal-age main sequence. Abundances and other details are the same as for the $4.21\mathrm{M}_\odot$ model considered in Section 3.1. At around 11 points along each evolutionary track, regularly spaced between the ZAMS and the red edge of the main sequence (REMS), we pass the stellar model to GYRE, which evaluates the model's eigenfrequencies and eigenfunctions for $\ell = 1$ and $\ell = 2$ g modes with radial orders up to $\tilde{n} \approx -100$.

Fig. 7 illustrates the location of the 312 models considered in the HR diagram. Each model is plotted as a circle; for those models that are unstable to one or more $\ell = 1$ (left-hand panel) or $\ell = 2$ (right-hand panel) g modes, the circle is shaded according to $\eta_{\max}$, the
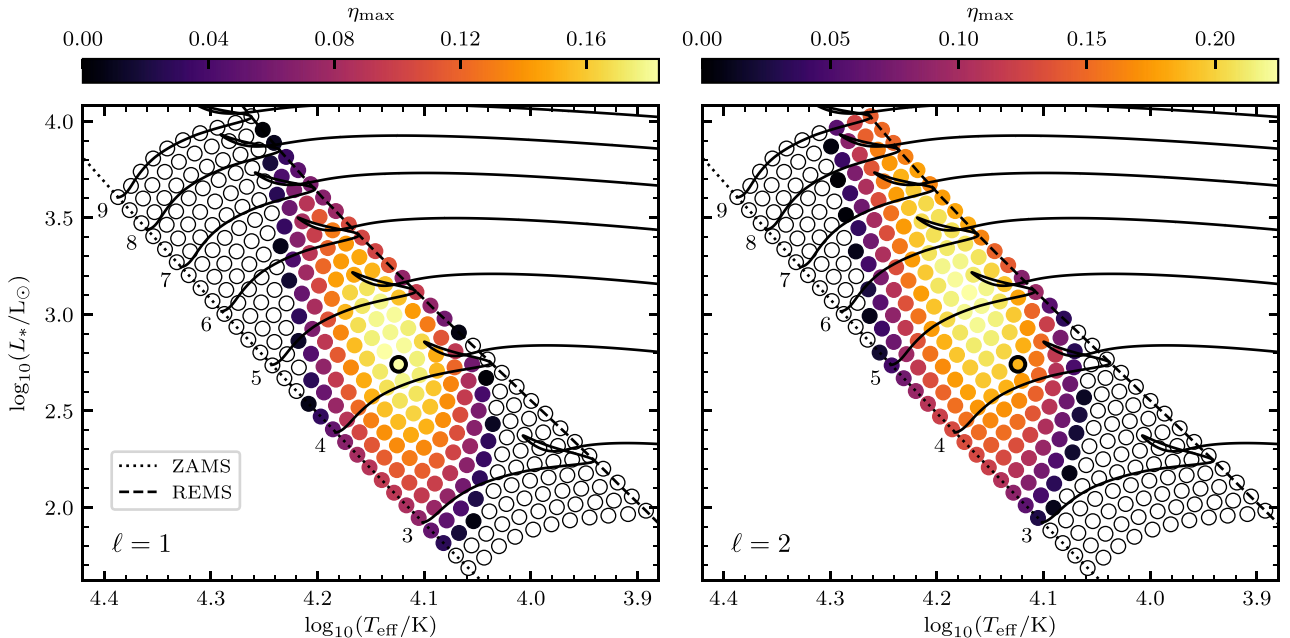

Figure 7. HR diagram showing the positions (circles) of the stellar models analysed using GYRE. Filled circles indicate stars in which one or more g-modes, with harmonic degrees $\ell = 1$ (left-hand panel) and $\ell = 2$ (right-hand panel), are unstable. The fill colour indicates the maximal value $\eta_{\max}$ of the normalized growth rate for the unstable modes. The bold circle indicates the $M = 4.21\mathrm{M}_\odot$ model studied in Section 3. Selected evolutionary tracks are plotted as solid lines, labelled on the left-hand side by the stellar mass in $\mathrm{M}_\odot$, and the ZAMS and red edge of the main sequence (REMS) are plotted as broken lines.
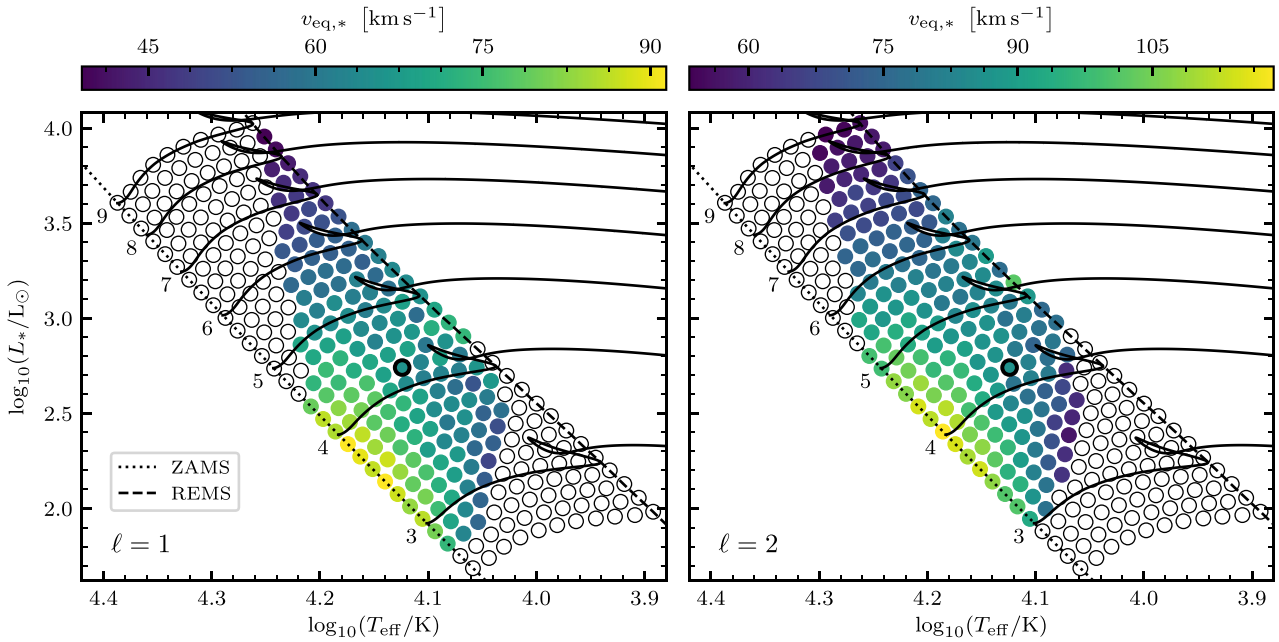
Figure 8. As in Fig. 7, except now that the fill colour indicates the surface equatorial rotation velocity $v_{\rm eq, *}$ established after 10^3 yr by the largest η unstable mode in the model.

maximal value attained by the normalized growth rate (21) across all unstable modes. The regions occupied by these shaded circles define the SPB instability strips, and show good agreement with previous studies (e.g. Pamyatnykh 1999; Miglio, Montalbán & Dupret 2007; Paxton et al. 2015). The $4.21{\rm M}_{\odot}$ model, highlighted with a bold circle, sits in the centre of the $\ell = 1$ strip – our motivation for selecting it as the focus of Section 3.

For each model harbouring unstable modes, we pick the mode with $\eta = \eta_{\rm max}$, evaluate the differential torque using equation (9) with $m = \ell$, and then simulate 10^3 yr of angular momentum transport following the procedure described in Section 3.4.1. Fig. 8 summarizes these simulations by reprising Fig. 7, but with the circles now shaded according to the surface equatorial velocity $v_{\rm eq, *}$ of the model at the end of the transport simulation. The figure confirms that the findings reported in Section 3.4 generalize to the SPB stars as a class. For the $\ell = 1$ modes, the equatorial velocities lie in the range 40–95 km s^{-1}. For the $\ell = 2$ modes, the range is somewhat larger, 50–120 km s^{-1}; the reasons for this were discussed in Section 3.4.4. Along a given evolutionary track, $v_{\rm eq, *}$ tends to decrease with age because the iron bump excitation region shifts deeper into the star where the moment of inertia is larger.

5 SUMMARY AND DISCUSSION

In the preceding sections, we have demonstrated that a single heat-driven g mode, excited to typically observed amplitudes, can establish a strong differential rotation profile within SPB stars, on time-scales ($\approx 10^3$ yr) that are extremely short compared to the stars' main-sequence evolution time-scales. In this section, we offer some caveats to provide necessary context for evaluating our findings, while at the same time highlighting possible avenues for future investigations. We then consider the wider implications of these findings, in particular focusing on current observational constraints on SPB-star rotation.

Our most significant caveat is that we do not account for the effects of rotation on the g modes – whether this rotation is initially present in the star, or arises as a consequence of angular momentum redistribution by the g modes themselves. Rotation influences the eigenfrequencies and eigenfunctions of g modes both by deforming the equilibrium stellar structure through the action of the centrifugal force and by directly modifying the governing oscillation equations. The latter modifications, which can have a significant impact even when the star is rotating at only a small fraction of the critical rate $\Omega_{\rm crit}$, take two forms. First, the inertial-frame eigenfrequency σ in equations (B1–B6) is everywhere replaced by its local corotating equivalent

$$\sigma_{\rm c} = \sigma - m\Omega. \tag{26}$$

This modification becomes important in the presence of differential rotation because $\sigma_{\rm c}$ is then a function of radial coordinate; in effect, the modes are progressively Doppler shifted as they propagate through regions of varying Ω. The result is to alter where in the star mode excitation and damping occur, and likewise where angular momentum is extracted and deposited. The impact of the Doppler shift is especially pronounced in critical layers where the real part of $\sigma_{\rm c}$ vanishes because the very short radial wavelength of modes then leads to significant dissipation (see, e.g. Booker & Bretherton 1967; Alvan, Mathis & Decressin 2013).

Secondly, rotation introduces extra terms in the linearized momentum equations (B2, B3) associated with the Coriolis acceleration. With these terms, the oscillation equations are no longer separable in r and θ, significantly complicating their solution. For the high-order g modes considered here, a common workaround is to adopt the so-called traditional approximation of rotation (TAR; see, e.g. Bildsten, Ushomirsky & Cutler 1996; Lee & Saio 1997; Townsend 2003, and references therein), which restores the r–θ separability of the oscillation equations by neglecting the horizontal component of the angular velocity vector in the Coriolis acceleration. The TAR has been applied successfully in the context of wave transport by stochastic IGWs (e.g. Pantillon, Talon & Charbonnel 2007; Mathis et al. 2008), and Mathis (2009) demonstrates one approach to generalize the TAR to work in differentially rotating stars.

Version 5.0 of GYRE implements the TAR and the Doppler effects described above. However, when these functionalities are enabled, mode eigenfunctions depend on the instantaneous rotation profile of the star, and must therefore be re-evaluated after each time-step of the angular momentum transport simulations (Section 3.4.1) – with the result that these simulations become significantly more computationally costly. With this in mind, we defer a full consideration of the effects of rotation to a future paper.

Another qualification concerns our focus (in the interests of simplicity) on angular momentum transport by a single pulsation mode. Although there are some SPB stars in which a single mode is dominant (see, e.g. De Cat et al. 2005), space-based photometry has revealed that there are also stars where hundreds of modes are simultaneously excited (albeit at smaller amplitudes). The combined torque from multiple modes will lead to angular velocity profiles more complex than the snapshots plotted in Fig. 3. Particularly important will be the competition between prograde/retrograde pairs of modes, having the same ℓ and $\tilde{n}$ but m values that differ in sign. Equation (9) indicates that such pairs will generate equal and opposite torques that exactly cancel; however, this symmetry is broken as soon as rotational effects are included, allowing one sense (e.g. prograde) to overcome the other.

Stochastic IGWs excited at convective core boundaries (Section 1) may also combine or compete with heat-driven g modes in transporting angular momentum. Correctly modelling these interactions will prove challenging; although a number of predictions have been made about the observable properties of stochastic IGWs in massive stars (e.g. Shiode et al. 2013; Aerts & Rogers 2015), there are no firm detections of these waves in SPB stars (Antoci 2014), and so the theoretical models remain poorly constrained by observations.

These caveats highlight the need for further theoretical work. Nevertheless, guided in part by the exploratory study by Townsend & MacDonald (2008), which incorporated Doppler shifts and multiple modes, we do not expect future investigations to overturn the qualitative aspects of our findings. We therefore turn now to an initial confrontation against observations. A key result of the Szewczuk & Daszyńska-Daszkiewicz (2015) analysis is that the surface rotation velocities of SPB stars appear to be systematically smaller than other B-type stars. We propose that this is a natural outcome if the total angular momentum content of SPB stars follows the same distribution as other B-type stars, but their surface layers have been spun down (and their interiors spun up) by prograde g modes. In support of our hypothesis, the recent study of five SPB stars by Pápics et al. (2017), based on data from the *Kepler* mission (Borucki et al. 2010), appears to confirm that the stars' variability is dominated by prograde modes.

Ideally, the *Kepler* data could be used to directly constrain the internal rotation of the Pápics et al. (2017) targets, and search for the differential rotation signature that our simulations predict. However, limitations in both observations and modelling mean that this has only been feasible in one case: the B8.3V star KIC 10526294, which exhibits zonal and retrograde dipole g modes in addition to prograde modes. By measuring the rotational splitting of a series of 19 dipole triplets with consecutive radial orders, Triana et al. (2015) infer the angular velocity profile throughout the star. Significantly, they find that the stellar interior ($x \lesssim 0.6$) is rotating in the opposite direction to outer regions – the same kind of counter-rotating profile as seen in the time snapshots of Fig. 3.

Nevertheless, a degree of caution should be exercised in directly linking this measurement to our findings. On one hand, the modes observed by Triana et al. (2015) have photometric amplitudes that are 1–2 orders of magnitude smaller than the ≈ 10 mmag implied by our choice of normalization (Section 3.2); and on the other hand, the inferred surface angular velocity of KIC 10526294, $\Omega \approx 0.8 \times 10^{-6}\,\mathrm{s}^{-1}$, is almost 100 times smaller than seen in the left-hand panel of Fig. 3. These differences for now prevent us from reaching firm conclusions about the origin of the counter-rotating profile in KIC 10526294, but it should be relatively straightforward to evaluate whether the combined torque exerted by the observed g-mode triplets can plausibly explain this profile.

On a final note, the foregoing discussion focuses on the results from our non-magnetic simulations. As the right-hand panel of Fig. 3 demonstrates, the field stresses generated by the TS dynamo effectively inhibit the strong differential rotation profile established by g modes. Based on simulations of rotation in magnetized stars (see, e.g. Mathis & Zahn 2005, and references therein), it is reasonable to suppose that *any* moderate field will be able to achieve the same outcome. This should apply whether the field is actively generated by the TS dynamo or another mechanism (e.g. the magnetorotational instability; Wheeler, Kagan & Chatzopoulos 2015), or is a fossil remnant from an earlier evolutionary stage; relevant to the latter case, around 7 per cent of B-type main-sequence stars are known to harbour stable, ordered magnetic fields with surface strengths $\gtrsim 100$ G, which are presumed to be fossils (Wade et al. 2014). It also remains possible that an as-yet-unknown angular momentum transport process (as for example invoked by Cantiello et al. 2014, to explain the slow core rotation of red giant stars) may play a role in determining whether g modes can establish a differential rotation profile.

REFERENCES

Aerts C., Rogers T. M., 2015, ApJ, 806, L33

Alvan L., Mathis S., Decressin T., 2013, A&A, 553, A86

Ando H., 1983, PASJ, 35, 343

Ando H., Osaki Y., 1977, PASJ, 29, 221

Antoci V., 2014, in Guzik J. A., Chaplin W. J., Handler G., Pigulski A., eds, Proc. IAU Symp. 301, Precision Asteroseismology. Kluwer, Dordrecht, p. 333

Ascher U., Mattheij R., Russell R., 1995, Numerical Solution of Boundary Value Problems for Ordinary Differential Equations. Soc. Ind. Appl. Math., Philadelphia

Asplund M., Grevesse N., Sauval A. J., Scott P., 2009, ARA&A, 47, 481

Belkacem K. et al., 2015, A&A, 579, A31

Bildsten L., Ushomirsky G., Cutler C., 1996, ApJ, 460, 827

Booker J. R., Bretherton F. P., 1967, J. Fluid Mech., 27, 513

Borucki W. J. et al., 2010, Science, 327, 977

Cantiello M., Mankovich C., Bildsten L., Christensen-Dalsgaard J., Paxton B., 2014, ApJ, 788, 93

Castor J. I., 1971, ApJ, 166, 109

Cowling T. G., 1941, MNRAS, 101, 367

De Cat P., Briquet M., Daszyńska-Daszkiewicz J., Dupret M. A., De Ridder J., Scuflaire R., Aerts C., 2005, A&A, 432, 1013

Denissenkov P. A., Pinsonneault M., 2007, ApJ, 655, 1157

Dunkerton T. J., 1981, J. Atmos. Sci., 38, 281

Dziembowski W. A., Moskalik P., Pamyatnykh A. A., 1993, MNRAS, 265, 588

Eddington A. S., 1926, The Internal Constitution of the Stars. Cambridge Univ. Press, Cambridge

Fuller J., Lai D., 2014, MNRAS, 444, 3488

Gastine T., Dintrans B., 2008a, A&A, 484, 29

Gastine T., Dintrans B., 2008b, A&A, 490, 743

Heger A., Langer N., Woosley S. E., 2000, ApJ, 528, 368

Kumar P., Quataert E. J., 1997, ApJ, 475, L143

Lee U., 2013, in Shibahashi H., Lynas-Gray A. E., eds, ASP Conf. Ser. Vol. 479, Progress in Physics of the Sun and Stars: A New Era in Helio- and Asteroseismology. Astron. Soc. Pac., San Francisco, p. 311

Lee U., Saio H., 1993, MNRAS, 261, 415

Lee U., Saio H., 1997, ApJ, 491, 839

Lee U., Neiner C., Mathis S., 2014, MNRAS, 443, 1515

Lee U., Mathis S., Neiner C., 2016, MNRAS, 457, 2445

Mathis S., 2009, A&A, 506, 811

Mathis S., Zahn J.-P., 2005, A&A, 440, 653

Mathis S., Talon S., Pantillon F.-P., Zahn J.-P., 2008, Sol. Phys., 251, 101

Meynet G., Maeder A., 1997, A&A, 321, 465

Miglio A., Montalbán J., Dupret M.-A., 2007, Comm. Astero., 151, 48

Pamyatnykh A. A., 1999, Acta Astron., 49, 119

Pantillon F. P., Talon S., Charbonnel C., 2007, A&A, 474, 155

Pápics P. I. et al., 2017, A&A, 598, A74

Paxton B., Bildsten L., Dotter A., Herwig F., Lesaffre P., Timmes F., 2011, ApJS, 192, 3

Paxton B., et al., 2013, ApJS, 208, 4

Paxton B., et al., 2015, ApJS, 220, 15

Rogers T. M., 2015, ApJ, 815, L30

Rogers T. M., MacGregor K. B., Glatzmaier G. A., 2008, MNRAS, 387, 616

Rogers T. M., Lin D. N. C., McElwaine J. N., Lau H. H. B., 2013, ApJ, 772, 21

Schatzman E., 1993, A&A, 279, 431

Shiode J. H., Quataert E., Cantiello M., Bildsten L., 2013, MNRAS, 430, 1736

Spruit H. C., 2002, A&A, 381, 923

Stellingwerf R. F., 1978, AJ, 83, 1184

Szewczuk W., Daszyńska-Daszkiewicz J., 2015, MNRAS, 450, 1585

Takata M., 2006, PASJ, 58, 893

Talon S., Charbonnel C., 2005, A&A, 440, 981

Talon S., Kumar P., Zahn J.-P., 2002, ApJ, 574, L175

Townsend R. H. D., 2003, MNRAS, 340, 1020

Townsend R., MacDonald J., 2008, in Bresolin F., Crowther P. A., Puls J., eds, Proc. IAU Symp. 250, Massive Stars as Cosmic Engines. Kluwer, Dordrecht, p. 161

Townsend R. H. D., Teitler S. A., 2013, MNRAS, 435, 3406

Triana S. A., Moravveji E., Pápics P. I., Aerts C., Kawaler S. D., Christensen-Dalsgaard J., 2015, ApJ, 810, 16

Unno W., Osaki Y., Ando H., Saio H., Shibahashi H., 1989, Nonradial Oscillations of Stars, 2 edn. Univ. Tokyo Press, Tokyo

Wade G. A. et al., 2014, in Petit P., Jardine M., Spruit H. C., eds, Proc. IAU Symp. 302, Magnetic Fields throughout Stellar Evolution. Kluwer, Dordrecht, p. 265

Waelkens C., 1991, A&A, 246, 453

Wheeler J. C., Kagan D., Chatzopoulos E., 2015, ApJ, 799, 85

Zahn J.-P., 1992, A&A, 265, 115

Zahn J.-P., Talon S., Matias J., 1997, A&A, 322, 320

Zahn J.-P., Brun A. S., Mathis S., 2007, A&A, 474, 145

APPENDIX A: UPDATES TO THE GYRE CODE

Since the initial release described by Townsend & Teitler (2013), the GYRE code has been significantly improved. In the context of this work, the most important addition is the ability to solve non-adiabatic oscillation problems; we describe this in greater detail in the following section. Other enhancements include implementations of the TAR (see Section 5) and the Cowling (1941) approximation (useful for comparison against existing calculations in the literature), the option of one-step initial-value integrators based on implicit Runge–Kutta schemes (e.g. Ascher, Mattheij & Russell 1995), which often prove more stable for non-adiabatic calculations than the Magnus method described in Townsend & Teitler (2013), adoption of the Takata (2006) classification scheme for dipole modes, development of a comprehensive test suite to provide code demonstration and validation, the ability to read stellar models in FGONG, OSC, and FAMDL formats, and improvements to the algorithm that sets up calculation grids, in particular, allowing stellar models that harbour density discontinuities. Moreover, GYRE is now fully integrated into the MESA project, and can be used to perform on-the-fly asteroseismic optimization (see Paxton et al. 2015, for details).

APPENDIX B: NON-ADIABATIC OSCILLATIONS

B1 Physical formulation

To model linear non-radial non-adiabatic oscillations, GYRE assumes perturbations of the form given in equation (7). The complex eigenfunctions $\tilde{\xi}_r$, $\tilde{\xi}_h$, etc. are found by solving the set of linearized conservation equations, comprising the continuity equation

$$\frac{\tilde{\rho}'}{\rho} + \frac{1}{r^2\rho}\frac{\mathrm{d}}{\mathrm{d}r}\left(r^2\rho\tilde{\xi}_r\right) - \frac{\ell(\ell+1)}{r}\tilde{\xi}_h = 0, \tag{B1}$$

the radial momentum equation

$$-\sigma^2\tilde{\xi}_r + \frac{1}{\rho}\frac{\mathrm{d}\tilde{P}'}{\mathrm{d}r} + \frac{\mathrm{d}\tilde{\Phi}'}{\mathrm{d}r} + \frac{\tilde{\rho}'}{\rho}g = 0, \tag{B2}$$

the horizontal momentum equation

$$-\sigma^2\tilde{\xi}_h + \frac{1}{r}\left(\frac{\tilde{P}'}{\rho} + \tilde{\Phi}'\right) = 0, \tag{B3}$$

Poisson's equation

$$\frac{1}{r^2}\frac{\mathrm{d}}{\mathrm{d}r}\left(r^2\frac{\mathrm{d}\tilde{\Phi}'}{\mathrm{d}r}\right) - \frac{\ell(\ell+1)}{r^2}\tilde{\Phi}' = 4\pi G\tilde{\rho}', \tag{B4}$$

the energy equation

$$-\mathrm{i}\sigma T\delta\tilde{S} = \delta\tilde{\epsilon} - \frac{1}{4\pi r^2\rho}\frac{\mathrm{d}\delta\tilde{L}_{\mathrm{rad}}}{\mathrm{d}r} + \frac{\ell(\ell+1)}{\mathrm{d}\ln T/\mathrm{d}\ln r}\frac{L_{\mathrm{rad}}}{4\pi r^3\rho}\frac{\tilde{T}'}{T} + \ell(\ell+1)\frac{\tilde{\xi}_h}{4\pi r^3\rho}\frac{\mathrm{d}L_{\mathrm{rad}}}{\mathrm{d}r}, \tag{B5}$$

and the radiative diffusion equation

$$\frac{\delta\tilde{L}_{\mathrm{rad}}}{L_{\mathrm{rad}}} = -\frac{\delta\tilde{\kappa}}{\kappa} + 4\frac{\tilde{\xi}_r}{r} - \ell(\ell+1)\frac{\tilde{\xi}_h}{r} + 4\frac{\delta\tilde{T}}{T} + \frac{1}{\mathrm{d}\ln T/\mathrm{d}\ln r}\frac{\mathrm{d}(\delta\tilde{T}/T)}{\mathrm{d}\ln r}. \tag{B6}$$

Here, T, S, L_{rad}, κ, and ϵ are the temperature, specific entropy, radiative luminosity, opacity and specific nuclear energy generation/loss rate, respectively, and other symbols were introduced in Section 2. Note that equation (B5) is obtained by neglecting the Lagrangian perturbation to the convective heating/cooling; see, e.g. equation 21.7 of Unno et al. (1989).

The linearized conservation equations are augmented by the thermodynamic identities

$$\frac{\delta\tilde{\rho}}{\rho} = \frac{1}{\Gamma_1}\frac{\delta\tilde{P}}{P} - \upsilon_T\frac{\delta\tilde{S}}{c_{\mathrm{P}}}, \qquad \frac{\delta\tilde{T}}{T} = \nabla_{\mathrm{ad}}\frac{\delta\tilde{P}}{P} + \frac{\delta\tilde{S}}{c_{\mathrm{P}}} \tag{B7}$$

and the perturbed opacity and energy generation relations

$$\frac{\delta\tilde{\kappa}}{\kappa} = \kappa_{\mathrm{ad}}\frac{\delta\tilde{P}}{P} + \kappa_{\mathrm{S}}\frac{\delta\tilde{S}}{c_{\mathrm{P}}} \qquad \frac{\delta\tilde{\epsilon}}{\epsilon} = \epsilon_{\mathrm{ad}}\frac{\delta\tilde{P}}{P} + \epsilon_{\mathrm{S}}\frac{\delta\tilde{S}}{c_{\mathrm{P}}}, \tag{B8}$$

where

$$\Gamma_1 = \left(\frac{\partial\ln P}{\partial\ln\rho}\right)_S \qquad \nabla_{\mathrm{ad}} = \left(\frac{\partial\ln T}{\partial\ln P}\right)_S \qquad \upsilon_T = -\left(\frac{\partial\ln\rho}{\partial\ln T}\right)_P \qquad c_{\mathrm{P}} = \left(\frac{\partial S}{\partial\ln T}\right)_P$$

$$\kappa_{\mathrm{ad}} = \left(\frac{\partial\ln\kappa}{\partial\ln P}\right)_S \qquad \kappa_{\mathrm{S}} = c_{\mathrm{P}}\left(\frac{\partial\ln\kappa}{\partial S}\right)_P \qquad \epsilon_{\mathrm{ad}} = \left(\frac{\partial\ln\epsilon}{\partial\ln P}\right)_S \qquad \epsilon_{\mathrm{S}} = c_{\mathrm{P}}\left(\frac{\partial\ln\epsilon}{\partial S}\right)_P. \tag{B9}$$

At the stellar origin ($r = 0$), boundary conditions are applied to enforce regular solutions. At the stellar surface ($r = R_*$), the boundary conditions are the vacuum condition

$$\delta\tilde{P} = 0, \tag{B10}$$

the requirement that the gravitational potential perturbation vanish at infinity,

$$(\ell+1)\frac{\tilde{\Phi}'}{r} + \frac{\mathrm{d}\tilde{\Phi}'}{\mathrm{d}r} = 0, \tag{B11}$$

and the perturbed Stefan–Boltzmann equation

$$\frac{\delta\tilde{L}_{\rm rad}}{L_{\rm rad}} = 2\frac{\tilde{\xi}_r}{r} + 4\frac{\delta\tilde{T}}{T}. \tag{B12}$$

B2 Dimensionless formulation

GYRE works with a dimensionless formulation of the linearized equations and boundary conditions given above. The independent variable is $x \equiv r/R_*$, and the dependent variables are a set of complex functions $y_i(x)$ $(i = 1, \ldots, 6)$ defined as

$$y_1 = x^{2-\ell}\frac{\tilde{\xi}_r}{r}, \qquad y_2 = x^{2-\ell}\frac{\tilde{P}'}{\rho g r}, \qquad y_3 = x^{2-\ell}\frac{\tilde{\Phi}'}{g r},$$

$$y_4 = x^{2-\ell}\frac{1}{g}\frac{\mathrm{d}\tilde{\Phi}'}{\mathrm{d}r}, \qquad y_5 = x^{2-\ell}\frac{\delta\tilde{S}}{c_{\rm P}}, \qquad y_6 = x^{-1-\ell}\frac{\delta\tilde{L}_{\rm rad}}{L_*}. \tag{B13}$$

With these definitions, the non-adiabatic pulsation equations are

$$x\frac{\mathrm{d}y_1}{\mathrm{d}x} = \left(\frac{V}{\Gamma_1} - 1 - \ell\right)y_1 + \left(\frac{\ell(\ell+1)}{c_1\omega^2} - \frac{V}{\Gamma_1}\right)y_2 + \frac{\ell(\ell+1)}{c_1\omega^2}y_3 + \upsilon_T y_5, \tag{B14}$$

$$x\frac{\mathrm{d}y_2}{\mathrm{d}x} = \left(c_1\omega^2 - A^*\right)y_1 + \left(A^* + 3 - U - \ell\right)y_2 - y_4 + \upsilon_T y_5, \tag{B15}$$

$$x\frac{\mathrm{d}y_3}{\mathrm{d}x} = (3 - U - \ell)y_3 + y_4, \tag{B16}$$

$$x\frac{\mathrm{d}y_4}{\mathrm{d}x} = UA^*y_1 + U\frac{V}{\Gamma_1}y_2 + \ell(\ell+1)y_3 + (2 - U - \ell)y_4 - \upsilon_T U y_5, \tag{B17}$$

$$x\frac{\mathrm{d}y_5}{\mathrm{d}x} = V\left[\nabla_{\rm ad}(U - c_1\omega^2) - 4(\nabla_{\rm ad} - \nabla) + c_{\rm dif}\right]y_1 + V\left[\frac{\ell(\ell+1)}{c_1\omega^2}(\nabla_{\rm ad} - \nabla) - c_{\rm dif}\right]y_2 + V\left[\frac{\ell(\ell+1)}{c_1\omega^2}(\nabla_{\rm ad} - \nabla)\right]y_3$$
$$+ V\nabla_{\rm ad}y_4 + [V\nabla(4 - \kappa_{\rm S}) + 2 - \ell]y_5 - \frac{V\nabla}{c_{\rm rad}}y_6, \tag{B18}$$

$$x\frac{\mathrm{d}y_6}{\mathrm{d}x} = \left[\ell(\ell+1)c_{\rm rad}\left(\frac{\nabla_{\rm ad}}{\nabla} - 1\right) - Vc_{\epsilon,\rm ad}\right]y_1 + \left[Vc_{\epsilon,\rm ad} - \ell(\ell+1)c_{\rm rad}\left(\frac{\nabla_{\rm ad}}{\nabla} - \frac{3 + \partial c_{\rm rad}}{c_1\omega^2}\right)\right]y_2 + \left[\ell(\ell+1)c_{\rm rad}\frac{3 + \partial c_{\rm rad}}{c_1\omega^2}\right]y_3$$
$$+ \left[c_{\epsilon,\rm S} - \frac{\ell(\ell+1)c_{\rm rad}}{\nabla V} + \mathrm{i}\omega c_{\rm thm}\right]y_5 - (\ell+1)y_6. \tag{B19}$$

Likewise, the boundary conditions are

$$\left.\begin{array}{r}c_1\omega^2 y_1 - \ell y_2 - \ell y_3 = 0\\ \ell y_3 - y_4 = 0\\ y_5 = 0\end{array}\right\}\text{at } x = 0, \qquad \left.\begin{array}{r}y_1 - y_2 = 0\\ (\ell+1)y_3 + y_4 = 0\\ (2 - 4\nabla_{\rm ad}V)y_1 + 4\nabla_{\rm ad}V y_2 + 4y_5 - y_6 = 0\end{array}\right\}\text{at } x = 1. \tag{B20}$$

In these expressions,

$$\omega \equiv \sqrt{\frac{R_*^3}{GM_*}}\sigma \tag{B21}$$

is the dimensionless frequency, while the other coefficients depend on the underlying stellar structure as follows:

$$V = -\frac{\mathrm{d}\ln P}{\mathrm{d}\ln r}, \qquad A^* = \frac{1}{\Gamma_1}\frac{\mathrm{d}\ln P}{\mathrm{d}\ln r} - \frac{\mathrm{d}\ln\rho}{\mathrm{d}\ln r}, \qquad U = \frac{\mathrm{d}\ln M_r}{\mathrm{d}\ln r}, \qquad c_1 = x^3\frac{M_*}{M_r},$$

$$\nabla = \frac{\mathrm{d}\ln T}{\mathrm{d}\ln P}, \qquad c_{\mathrm{rad}} = x^{-3}\frac{L_{\mathrm{rad}}}{L_*}, \qquad \partial c_{\mathrm{rad}} = \frac{\mathrm{d}\ln c_{\mathrm{rad}}}{\mathrm{d}\ln r}, \qquad c_{\mathrm{thm}} = \frac{4\pi R_*^3 c_{\mathrm{P}} T\rho}{L_*}\sqrt{\frac{GM_*}{R_*^3}},$$

$$c_{\mathrm{dif}} = (\kappa_{\mathrm{ad}} - 4\nabla_{\mathrm{ad}})\, V\nabla + \nabla_{\mathrm{ad}}\left(\frac{\mathrm{d}\ln\nabla_{\mathrm{ad}}}{\mathrm{d}\ln r} + V\right),$$

$$c_{\epsilon,\mathrm{ad}} = \frac{4\pi R_*^3\rho\epsilon}{L_*}\epsilon_{\mathrm{ad}}, \qquad c_{\epsilon,S} = \frac{4\pi R_*^3\rho\epsilon}{L_*}\epsilon_{\mathrm{S}}, \tag{B22}$$

with M_r the mass interior to radius r.

This paper has been typeset from a TEX/LATEX file prepared by the author.